On the ability of dual-polarimetric SAR measurements to observe lava flows under different volcanic environments

Emanuele Ferrentino [a,*], Christian Bignami [a], Ferdinando Nunziata [b], Salvatore Stramondo [a], Maurizio Migliaccio [a,b]

[a] *Istituto Nazionale di Geofisica e Vulcanologia, Via di Vigna Murata, 605, Roma, 00143, Italy*
[b] *Università degli Studi di Napoli Parthenope, Centro Direzionale isola C4, Napoli, 80143, Italy*

ARTICLE INFO

ABSTRACT

In this study, we discuss the extra-value of polarimetric information in observing the lava flow. Dual-polarimetric Synthetic Aperture Radar (SAR) measurements are processed using a polarimetric change detector that, instead of looking at the variation of the backscatter intensity between a pair of images collected before and after the event, looks at changes in the polarimetric scattering behavior. We demonstrate that the scattering changes detected by the proposed polarimetric approach well-correlate with the footprint of the lava flow provided by external sources. In addition, we also compare the performance of the polarimetric change detector with conventional single-polarization metrics showing that the former always outperforms the incoherent single-polarization measurements. To further demonstrate the robustness of the polarimetric change detectors, we selected two test cases that refer to vulcanic eruptions calling for completely different environments. The first one, related to the Etna volcano, calls for a lava flow over a vegetation-free environment; the second one is related to the Nyiragongo volcano and calls for a lava flow in a vegetated environment. Experimental results show that the polarimetric change detectors automatically adapt to the changing environment outperforming the single-polarization detectors.

1. Introduction

Lava flows mapping during or after an eruption is an important step for crisis management and post-disaster emergency response to reduce the impact of the volcanic eruptions. A fast lava flow map can be fundamental to provide a better tracking and emplacement evolution, and, therefore, to mitigate human losses and casualties. This information is also one of the multiple factors to evaluate the volcanic hazards for supporting decision-makers and all the authorities involved in the risk management chain.

Within this context, remotely sensed measurements play a key role in providing detailed information on the lava flow. Optical sensors, with high and very high spatial resolution measurement capabilities, can be accessed easily and their measurements can be interpreted even by non-trained personnel. Nevertheless, the effects of atmospheric agents and solar illumination severely impact optical radiation. In addition, during an eruption, a mix of water vapor, ashes, carbon dioxide, and sulfur gases that compose the volcanic plume, comes out of the eruptive vent hampering ground observations. Radar sensors can help to mitigate these issues by ensuring continuous observations over wide areas nearly in all-weather conditions. Particularly, the Synthetic Aperture Radar (SAR) is of fundamental importance to monitor lava activity because of its fine spatial resolution and the capacity of microwaves to penetrate volcanic plumes.

SAR-based change detection (SAR-CD) is a robust method to map changes due to natural disasters (Bovolo and Bruzzone, 2005; Ferrentino et al., 2021) and this rationale can be also used for volcanic applications. With respect to volcanic eruptions L-, C-, and X-band SAR imagery have been effectively employed to detect and map lava flows. In Zebker et al. (1996), a time series of C-band SIR-C SAR imagery is used to analyze lava flows over the Kilauea volcano, Hawaii. Experimental results, obtained using interferometric coeherence, show that the lava flow results in a loss of coherence. Dietterich et al. (2012) exploits the loss of the coherence to map the lava flow due to the eruption of the Kiluauea volcano using C-band ENVISAT-ASAR imagery. Coherence changes are also used in Lee et al. (2023) where a set of C-band Sentinel-1 SAR data are exploited to detect the lava emplacement of the 2018 Kilauea eruption. Results confirm that coherence change detection is an effective method even though it requires a

---

short revisit time of satellite acquisitions to limit the coherence loss due to temporal and spatial baseline. In Bignami et al. (2014) a fast color composite representation is used to process a time series of C-band intensity SAR imagery acquired by the ENVISAT-ASAR to map the lava deposit emplacement during the large eruption of Cordon-Caulle Volcano (Chile). In Bignami et al. (2013), X-band COSMO-SkyMed (CSK) SAR imagery are processed using a normalized change index (NCI) to provide information about the pyroclastic density current (PDC) deposits occurred during the 2010 Merapi volcanic eruption. Results show that the variation of the normalized radar cross section (NRCS) is a proxy of PDC deposits. In Bignami et al. (2020), a time series of C-band Sentinel-1 (S-1) and X-band CSK SAR imagery collected after the 2014–2015 Fogo volcanic eruption, in Capo Verde, is processed by jointly exploiting interferometric coherence and intensity metrics to observe the lava field and to track its evolution in an unsupervised way. Results show that the lava field and its temporal evolution can be automatically estimated. In Dualeh et al. (2021), X-band CSK SAR imagery collected after the June 3, 2018 eruption of Fuego volcano, Guatemala, is used to analyze the backscattering signal associated to explosive volcanic deposits. Results demonstrate a sensitivity of CSK SAR measurements to PDC deposits. In Plank et al. (2023) a method based on Digital Elevation Model (DEM) differentiation is proposed to estimate the volume of the lava using both optical and SAR very high-resolution images acquired under the bistatic geometry by the TanDEM-X SAR mission. The method requires high-resolution and very high-resolution data that are not always available and the bi-static geometry is the only way to get accurate DEM from SAR measurements. These features limit the applicability of this method. In Palamà et al. (2023) a radargrammetry approach is proposed to map the lava field related to the La Palma eruption in 2021. The approach is applied to very high resolution (less than 1 m) SAR imagery acquired by the X-band Capella Space mission. The performance of the approach depends on an adequate choice of the spatial baseline of the SAR image pair.

In recent years, an increasing number of SAR missions equipped with multiple polarization modes has been launched. As a consequence, new added-value products have been proposed in different thematic domains, e.g. forests, land, urban areas, and oceans (Migliaccio et al., 2011; Migliaccio and Nunziata, 2014; Nunziata et al., 2019; Migliaccio et al., 2021; Ferrentino et al., 2022; Polcari et al., 2023). However, only few studies deal with polarimetric SAR measurements to observe volcanic eruption. In Weissel et al. (2004), a classification scheme based on the identification of the dominant scattering mechanism is applied to a full-polarimetric (FP) AIRSAR L-Band SAR image collected during the early stages of the 1996 Manam Volcano, Papua New Guinea eruption sequence. Experimental results show the role of polarimetric information to distinguish recent lava flows. In Solikhin et al. (2015), co- and cross-polarized L-band ALOS-PALSAR SAR data are exploited to detect changes after the 2010 Merapi eruption, Indonesia, demonstrating that the NRCS measured using the two polarimetric channels carry out complementary information. In Poland (2022), dual-polarimetric (DP) C-band RadarSAT-2 and S-1 imagery are processed to map the volcanic mass flows by jointly using amplitude and coherence evaluated using the cross-polarized channel. The study demonstrates the key role of the cross-polarized channel in detecting the lava flow in vegetated areas. In Rogic et al. (2023), airborne multi-frequency (L- and S-band) FP SAR measurements, are used to classify volcanic terrain around Mount St. Helens. The approach uses intensity information to map soil roughness and, therefore, to identify volcanic terrains. In Corradino et al. (2021), SAR measurements acquired by Sentinel-1 sensor are used together with optical measurements to analyze the 2018 Mount Etna eruption and the 2014–2015 Fogo Island eruption. The approach is based on a k-means classifier applied to DP VV-VH SAR measurements collected over the Etna case study and single-polarization (SP) VV SAR measurements collected over the Fogo Island test case. The analysis of the state-of-the-art shows that only few studies used polarimetric SAR measurements to observe volcanic events and the adopted metrics are mainly based on the incoherent channels, i.e.; no inter-channel phase information is exploited.

In this study, the benefit of coherent dual-polarimetric SAR measurements to observe lava flow is investigated using metrics that exploit both intensity and inter-channel phase information. A polarimetric change detector (CD) is proposed to enhance the scattering changes between a pair of DP SAR imagery collected before and after the volcanic eruption. To better assess the performance of the DP CD, conventional SP metrics are used. Then, both DP and SP metric are processed using a constant false alarm rate (CFAR) approach to provide a binary map that identifies the lava flow. The detected lava flow is then contrasted with a lava footprint obtained by external sources. The performance analysis, carried on both quantitatively and in a qualitative way using figure of merits, shows that the DP CD always outperforms SP metrics. Two case studies are analyzed that call for completely different volcanic conditions. The first one deals with the 2018 Etna, Italy, volcanic eruption and consists of distinguishing the lava from a vegetated-free surroundings under steep slope conditions. The second one deals with the 2021 Nyiragongo, the Democratic Republic of the Congo, eruption and consists of estimating the lava against a vegetation-covered surroundings under gentle slope conditions.

2. Test sites and dataset

In this section, the two test sites and the dataset are described.

2.1. Mount Etna Eruption - 24 December 2018

Mount Etna is recognized as one of the most active volcanoes worldwide and it is located on the eastern coast of Sicily, in close proximity to the metropolitan city of Catania. The monitoring of Mount Etna is of paramount importance due to the potential hazards it poses for approximately 900,000 people living on its slopes and the hundreds of thousands of tourists who visit the volcano annually (Bisson et al., 2021). In the last 50 years, Mount Etna has been erupting more frequently and releasing larger volumes of magma. One of the most recent violent eruptions occurred on 24 December 2018 from a 2-km-long fissure opened on the volcano's south-eastern (SE) flank at 3300 m above sea level spewing lava and sending up plumes of ash (Cannavo' et al., 2019). During the Strombolian eruption, volcanic vents spewed lava fountains that led to the formation of a dense, ash-laden plume, and lava flowed down several areas of the Valle del Bove. In the afternoon, the explosive activity decreased ending the night between 24 and 25 December. However, the lava flows fed up to 27 December covering an area around 1 km^2 (Cannavo' et al., 2019), see Fig. 1(a). The optical image of Fig. 1(a) shows that the area surrounding the lava flow mainly consists of vegetation-free rocky areas.

Unfortunately, no ground information are available. Hence, to test the performance of the multi-polarization metrics we considered the contour of the lava flow provided by Copernicus EMS (CEMS). This contour map is considered as benchmark since it was obtained by visually inspecting the post-event very high resolution Pléiades-1A/B satellite image collected on 27 December 2018 by trained personnel (CEMS, 2019). The lava flow footprint is superimposed in red on the optical image of Fig. 1(a).

The SAR dataset consists of a pair of C-band S-1 Interferometric Wide (IW) imagery collected over the Mount Etna before (22 December, 2018) and after (28 December, 2018) the eruption event. The S-1 data are acquired in ascending pass with an angle of incidence of around 36°, see Table 1. The speckle filtered imagery are shown in Fig. 2 where the rows displaying the VV (panels (a) and (b)) and the VH (panels (c) and (d)) NRCS, while columns stand for pre- (panels (a) and (c)) and post-eruption (panels (b) and (d)). For reference purpose, the EMS footprint is also annotated in red on both the pre- and post-event imagery.
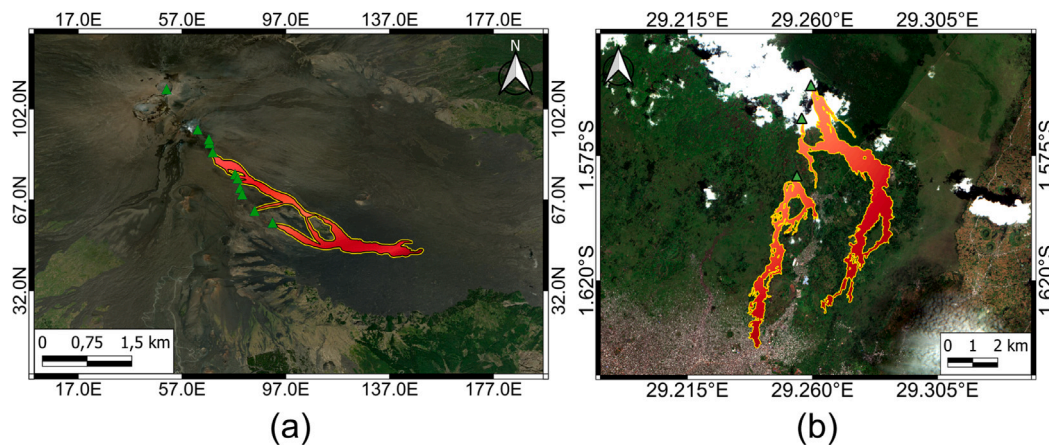
Fig. 1. Optical image collected over the Etna (a) and Nyiragongo (b) volcano. The footprint of the lava flow provided by Copernicus EMS is superimposed in red for reference purposes. The green triangles stand for volcanic vents. (For interpretation of the references to color in this figure legend, the reader is referred to the web version of this article.)

Table 1
Sentinel–1 SAR data set.

| Acquisition date	Resolution (range × azimuth) (m)	Acquisition mode	Polarization	Angle of incidence	Volcano (Eruption date)
22 December, 2018	2.33 × 13.92	Ascending	DP (VV+VH)	≈36°	Etna (24 December 2018)
28 December, 2018	2.33 × 13.92	Ascending	DP (VV+VH)	≈36°	Etna (24 December 2018)
13 May, 2021	2.33 × 14	Ascending	DP (VV+VH)	≈36°	Nyiragongo (22 May 2021)
25 May, 2021	2.33 × 14	Ascending	DP (VV+VH)	≈36°	Nyiragongo (22 May 2021)
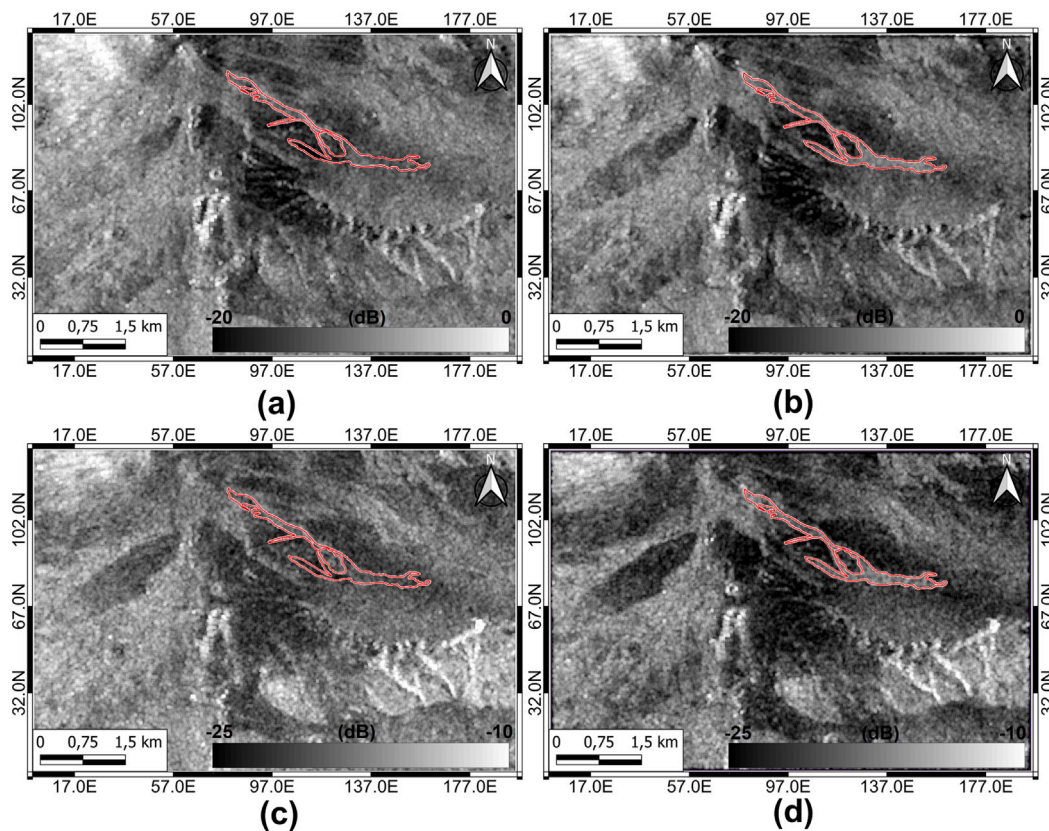
Fig. 2. Excerpts of the S-1 SAR imagery collected over the Mount Etna. The figure is organized in a matrix format where the rows correspond to the VV ((a) and (b)) and VH ((c) and (d)) channels while columns correspond pre- ((a) and (c)) and post-eruption ((b) and (d)). The area affected by lava flow is enclosed in the red EMS footprint in both the pre- and post-event imagery.

Fig. 3. Excerpts of the S-1 SAR collected over the Mount Nyiragongo. The figure is organized in a matrix format where the rows correspond to the VV ((a) and (b)) and VH ((c) and (d)) channels while columns correspond pre- ((a) and (c)) and post-eruption ((b) and (d)). The area affected by lava flow is enclosed in the red EMS footprint in both the pre- and post-event imagery.
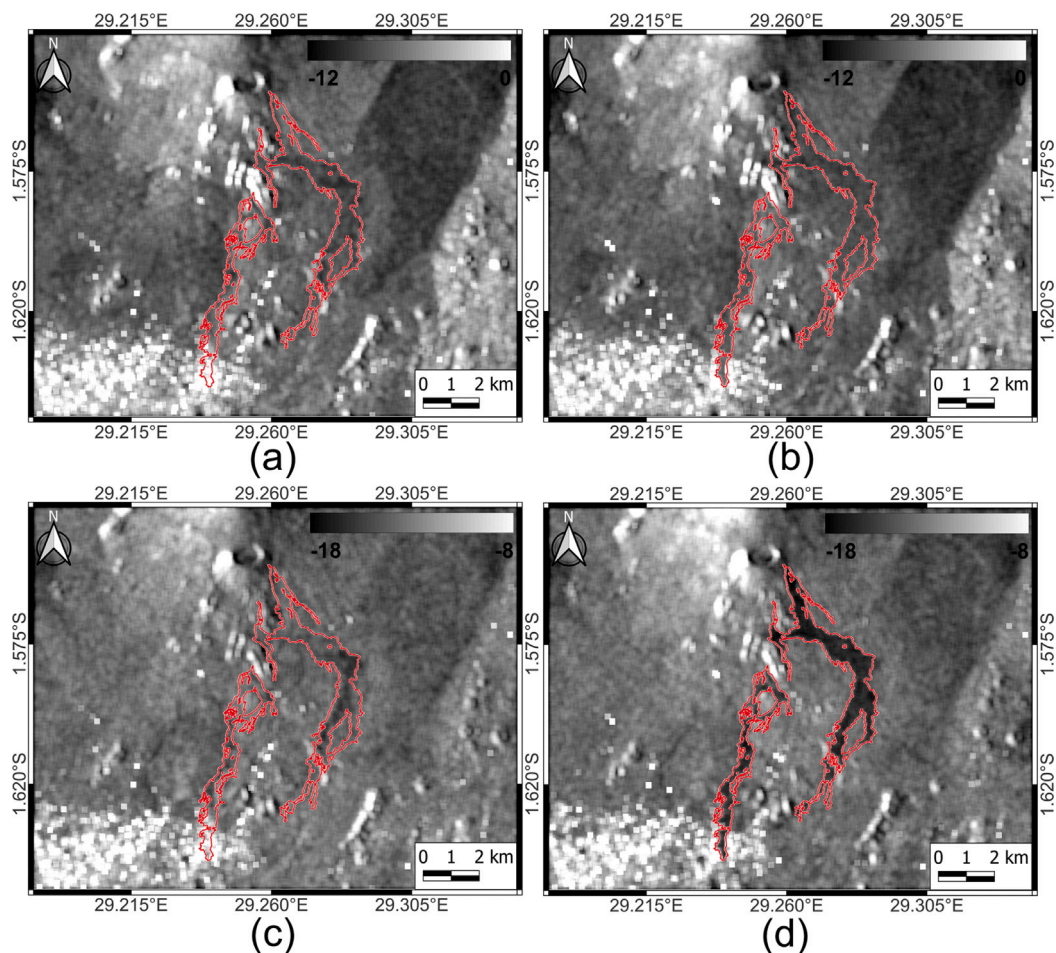
2.2. Mount Nyiragongo Eruption - 22 May 2021

The Mount Nyiragongo is an active stratovolcano located inside Virunga National Park, in the Democratic Republic of the Congo, which is almost permanently active and it is famous for the largest summit lava lake in the world (Boudoire et al., 2022). On 22 May 2021, the volcano erupted resulting in a lava that flew toward south hitting the city of Goma destroying several neighborhoods and infrastructure, including roads, bridges, and buildings. As a consequence, 450,000 people were displaced and evacuated while 32 people died and 1000 houses were destroyed (Boudoire et al., 2022).

Even in this case, no ground information is available; therefore we select for benchmark purposes the contour of the lava flow provided by Copernicus EMS and derived by trained personnel who visually inspected the Multi Temporal and Coherence (MTC) map obtained from COSMO-SkyMed Stripmap Himage post-event satellite images collected on 29/05/2021 and 30/05/2021 (CEMS, 2021). The lava flow footprint is superimposed in red on the optical image of Fig. 1(b) which also shows that the area affected by the eruption is largely covered by vegetation.

The SAR dataset consists of a pair of C-band S-1 Interferometric Wide (IW) imagery collected over the Mount Nyiragongo before (13 May, 2021) and after (25 May, 2021) the eruption event. The S-1 data are acquired in ascending pass with an angle of incidence of around 36°, see Table 1. The speckle filtered imagery are shown in Fig. 3 where the rows correspond to the VV (panels (a) and (b)) and VH (panels (c)

and (d)) channels while columns correspond pre- ((a) and (c)) and post-eruption ((b) and (d)). For reference purpose, the EMS footprint is also annotated in red on both the pre- and post-event imagery.

3. Theoretical background

3.1. Dual-polarimetric change detector

In this section, the theoretical rationale that underpins the proposed DP CD is described, see the schematic of Fig. 4.

The goal of the DP CD is to emphasize the scattering changes occurred after the eruption using a pair of DP SAR imagery collected before and after the eruption. The polarimetric CD metric is based on the methodology proposed in Ferrentino et al. (2019b) and Marino and Nannini (2022) which consists on the ratio of the pre- to post-event covariance matrices both estimated using a 5×5 boxcar window:

$$\mathbf{C}_{CD} = \mathbf{C}_2 \mathbf{C}_1^{-1} \tag{1}$$

where $\mathbf{C}_1$ and $\mathbf{C}_2$ are the covariance matrices collected at two different times, but with identical geometry and related to the same observed scene. The key idea is finding the scattering mechanisms $\underline{\omega}$ that maximize $\mathbf{C}_{CD}$ (1), i.e.; the scattering basis that emphasizes the changes from the pre- to the post-event imagery. To perform this task, the Lagrange optimization procedure is used (Marino and Nannini, 2022; Ferrentino et al., 2019b) that results in the following eigenvalue problem:

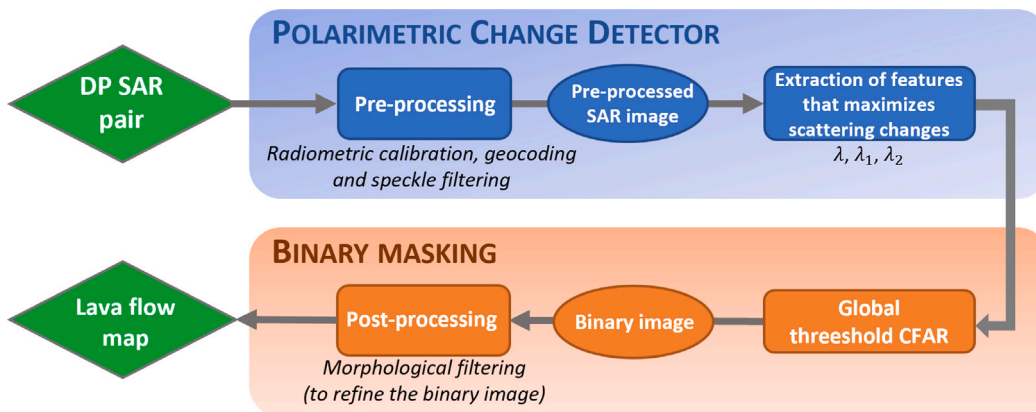$$\mathbf{C}_{CD}\omega = \lambda_i \underline{\omega} \tag{2}$$

Fig. 4. Schematic diagram of the proposed rationale.
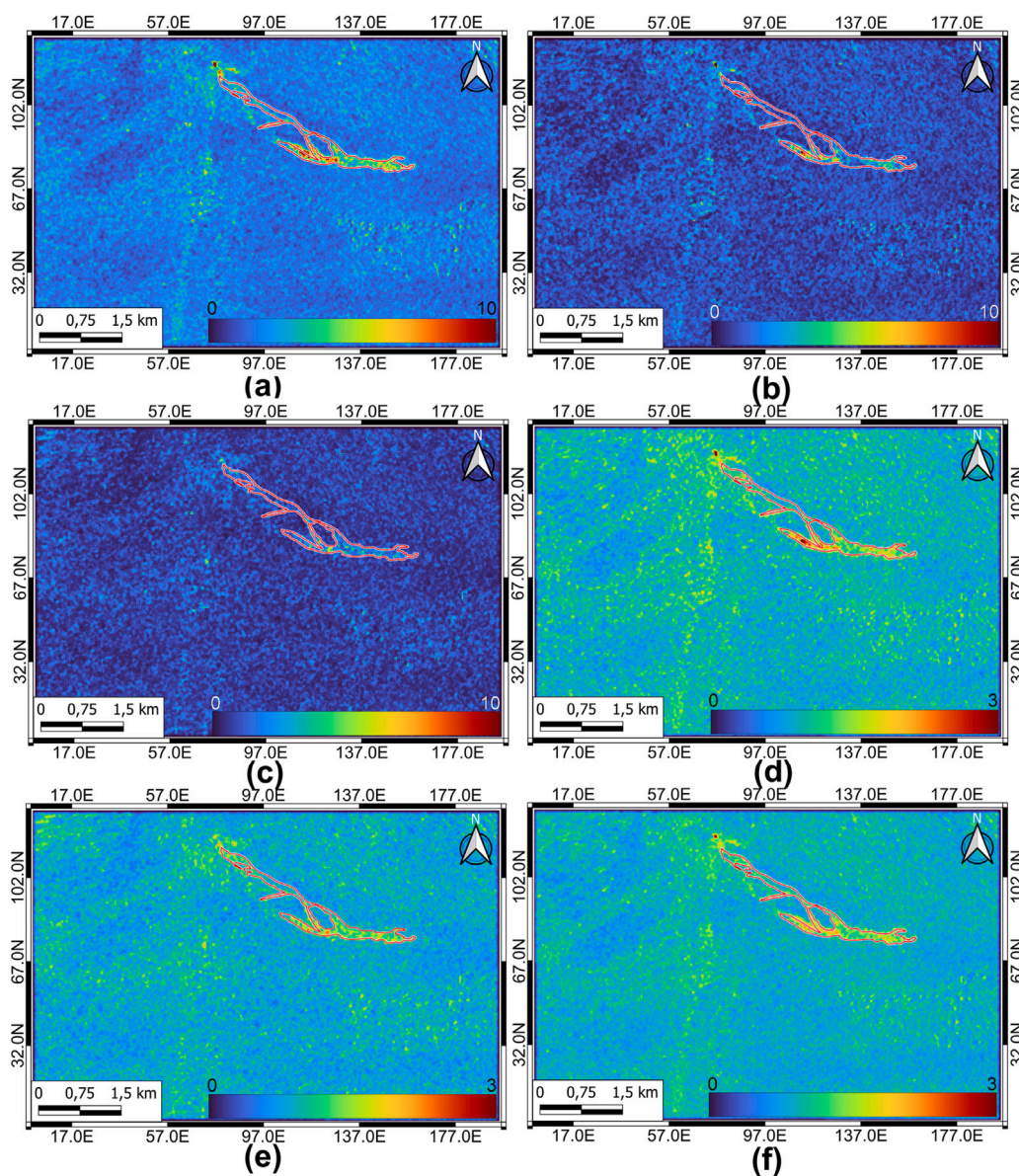
Fig. 5. False color change detection map that refers to an excerpt of the SAR acquisitions over the Mount Etna: (a) λ; (b) λ_1; (c) λ_2; (d) $R_{i_{VV}}$; (e) $R_{i_{VH}}$; and (f) $R_{i_{VVVH}}$. The lava flow area is enclosed in the red EMS footprint. (For interpretation of the references to color in this figure legend, the reader is referred to the web version of this article.)
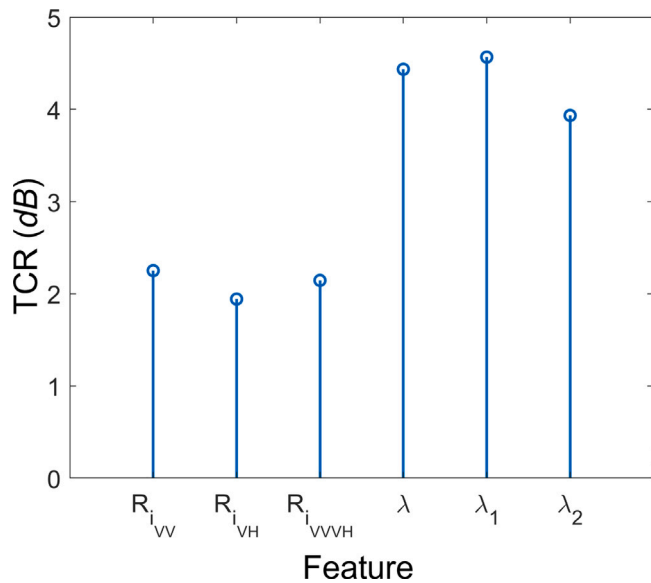
Fig. 6. TCR evaluated over Mount Etna considering the lava flow and an equal-size ROI belongings to the surrounding environment.

where λ_i (with $i = 1, 2$) are the real eigenvalues that optimize $\mathbf{C}_{CD}$.

In this study, the metrics adopted to analyze the changes are the two eigenvalues λ_1 and λ_2 and their sum $\lambda = \lambda_1 + \lambda_2$.

3.2. Generation of the binary mask

To assess the performance of the CD in a fair way, we generate a binary map related to the observed lava flow that is eventually contrasted with the benchmark lava footprint provided by Copernicus EMS. In this study, the clutter is defined as the environment that does not belong to the lava flow. This means that, in general, a quite heterogeneous clutter is to be expected that would suggest using an adaptive CFAR approach based on local thresholding. However, in this study, a sub-optimal global-threshold CFAR is used since the main goal is to analyze the benefits of polarimetric information with respect to single-polarization channels. A better design of the detection phase can be used to improve the binary mask obtained but it does not affect the ranking of polarimetric information in observing lava flow. To design a CFAR detector, the statistics of the clutter must be analyzed. The empirical probability density function (pdf) is evaluated over a region of interest (ROI) that surrounds the lava flow and the Kolmogorov–Smirnov binary test, performed using a significance level equal to 0.05, shows that the clutter is approximately Lognormal distributed for all the metrics. This means that a closed-form relationship between the probability of false alarm (P_{fa}) and the threshold th is available (Ferrentino et al., 2019a):

$$P_{\text{fa}} = \int_{\text{th}}^{\infty} \frac{1}{x\sigma\sqrt{2\pi}} e^{-\frac{(\ln(x)-\mu)^2}{2\sigma^2}} \, \mathrm{dx} \tag{3}$$

where the threshold is given by:

$$\text{th} = e^{\sqrt{2}\sigma \text{erf}^{-1}(1-2P_{\text{fa}})} \tag{4}$$

with μ and σ being the mean and standard deviation of the Lognormal distribution, respectively and $\text{erf}(\cdot)$ stands for the error function. Hence, the binary image is simply obtained by comparing each metric with the threshold (4).

4. Experiments

The first test consists of the analysis of the SAR pair related to the December 2018 Etna eruption (see Table 1). The Mount Etna is

largely made up of rocky and unvegetated areas, hence, this showcase is to discuss the ability of the polarimetric CD to observe the lava flow against a non-vegetated background. A close view of the VV- and VH-polarized ground-projected SAR images, which includes the area of interest, is shown in Fig. 2. By visually contrasting the SAR images acquired before (first column) and after (second column) the eruption, it is hard to distinguish the area affected by the lava in both the channels. By superimposing the EMS footprint on the pre- and post-event imagery we can note that the lava results in a slightly larger backscattered signal in both co- and cross-polarized post-event imagery, with the co-polarized image resulting in the largest increase of the backscattering, see Fig. 2(a). This suggests investigating the joint use of co- and cross-polarized channels according to the proposed multi-polarization approach.

The metrics λ_1, λ_2 and λ are shown in Fig. 5(a), (b) and (c), respectively, in false colors and the area affected by the changes is again included in the red EMS polygon. By visually inspecting those images, one can see that the lava flow is well emphasized with respect to the clutter. The λ_1 (a) and λ (c) images result in the best contrast between the lava and its surroundings; while in the λ_2 image (b) the contrast appears weaker. This, again, points out the different sensitivity of the co- and cross-polarized channels to the backscatter from the lava and the surrounding environment. In fact, λ_1 and λ_2 carry on information related to the changes in the backscatter measured in the co- and cross-polarized channels, respectively; while λ is intimately related to the changes occurred in to the total backscattered power. In summary, the visual analysis suggests that the lava flow is brighter in the co-polarized channel; while its surroundings are darker in the cross-polarized one. In addition, the scattering behavior of the lava results in some well-distinguishable complementarities.

To discuss the performance of the DP metrics with respect to single-polarization ones, a SP feature, based on the pre- and post-event NRCS ratio, is used as reference:

$$R_i = \frac{i_{post}}{i_{pre}} \tag{5}$$

where i stands for the NRCS calculated using the co- and cross-polarized channels:

$$\begin{aligned} i_{vv} &= \sigma_{vv}^0 \\ i_{vh} &= \sigma_{vh}^0 \end{aligned} \tag{6}$$

and using the total backscattered power, namely the SPAN:

$$i_{vvvh} = \sigma_{vv}^0 + \sigma_{vh}^0 \tag{7}$$

The outputs related to $R_{i_{vv}}$, $R_{i_{vv}}$ and $R_{i_{vvvh}}$ are shown in Fig. 5(d), (e) and (f), respectively where the area affected by the changes is enclosed in the reference EMS footprint. The visual inspection of those metrics show that changes in the lava-affected area can be hardly observed. In addition, the contrast between the metric evaluated within the lava-affected area and its surroundings appear quite weak.

To quantify the ability of multi-polarization metrics in emphasizing the lava flow, the target-to-clutter ratio (TCR) is used (Muhammad et al., 2022):

$$TCR = 10 \cdot log_{10}\left(\frac{X_t}{X_c}\right) \tag{8}$$

where $X \in \left\{R_{i_{VV}}, R_{i_{VH}}, R_{i_{VVVH}}, \lambda, \lambda_1, \lambda_2\right\}$ is the mean value of the metric evaluated within the lava flow (subscript t) and the clutter (subscript c), respectively. Results, depicted in Fig. 6, show that the DP metrics outperform the SP ones in emphasizing the lava flow with respect to the soundings, with λ_1 performing best. DP features provide a separability around 2 dB larger than the SP ones, suggesting a key role of coherent polarimetric information to observe this volcanic phenomenon. It is also worth noting that λ, although related to the SPAN, provides a TCR different from $R_{i_{VVVH}}$. This witnesses the
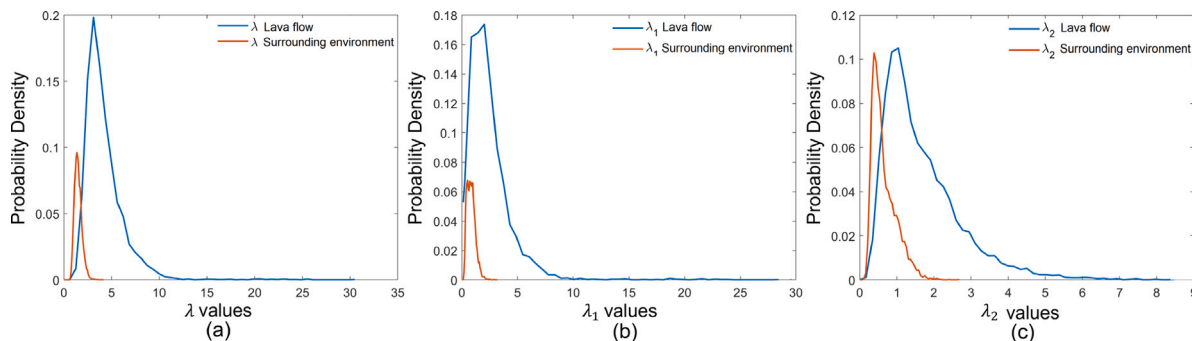
Fig. 7. Empirical pdfs evaluated using the metrics λ (a), λ_1 (b) and λ_2 (c) evaluated within an area affected by lava flow (blue color) and the surrounding environment (red color). (For interpretation of the references to color in this figure legend, the reader is referred to the web version of this article.)
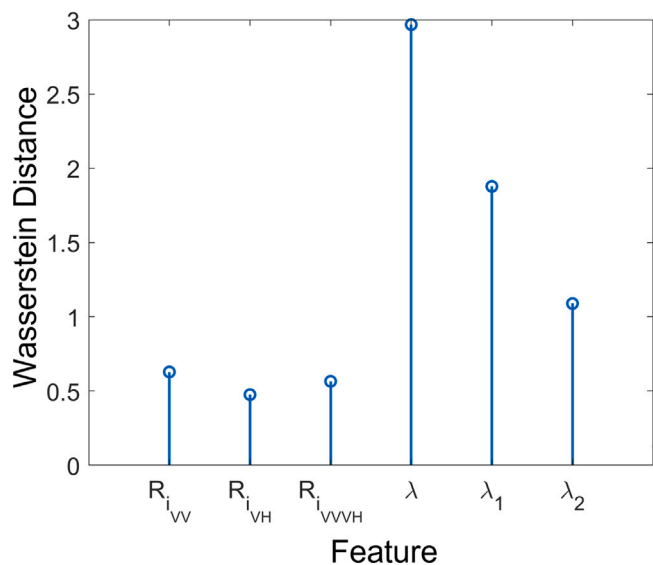

Fig. 8. Wasserstein distance evaluated over Mount Etna using both DP and SP features.

key role played by the optimization procedure (2) that maximizes the scattering changes between the pre- and post-event scans.

Finally, the CFAR detector is applied to extract the lava flow. To select the best metric to be processed by the CFAR, a statistical analysis is carried out on each DP metric to assess the separability of the lava flow from its surroundings. The pdfs of the DP metrics are depicted in Fig. 7 in blue (lava) and red (clutter) colors. The best separability is provided by λ which is, therefore, more robust than λ_1 in separating the target from the clutter from a statistical viewpoint. To quantify this separability, the Wasserstein distance (Vallender, 1974) is evaluated and depicted in Fig. 8 where the distance evaluated using the SP metrics is also annotated for reference purposes. The distance confirms that the best separability is given by λ, with a probability distribution distance three times larger than the SP metrics.

The CFAR is applied to λ and, according to Eq. (4), *th* is evaluated using a P_{fa} equal to 10^{-5} that resulted in the best compromise between detection accuracy and false alarms. Morphological filtering is also applied to refine the output by removing artifacts and filling holes. The binary image output is superimposed in red on the optical image and shown in Fig. 9(a) where, once again, a good spatial agreement with the reference lava flow depicted in blue can be observed. However, it can be noted that most of the lava flow is detected in the bottom part of the image, while the lava located in the upper part is not well detected. This suggests an analysis of the effect of the slope in lava flow detection. The slope, evaluated using the 30 m Shuttle Radar Topography Mission (SRTM) Digital Elevation Model (DEM), is depicted in Fig. 9(b) showing

that the area under investigation calls for very steep slopes ranging from 0° up to 70°. The Google Earth three-dimensional reconstruction of Mount Etna, shown in Fig. 9(c) where the Copernicus EMS reference footprint is superimposed and shown in red, highlights that the area where the lava flow is not well-detected belongs to the area calling for steep slope. On the other side, the lava is well-detected in the gentle slope area, i.e., in the area where the concentration of the lava increases due to the topography that is less steep (the so-called accumulation zone). This suggests to discuss the behavior of the co- and cross-polarized backscatter signals with respect to the slope in both the pre- and the post-event imagery. The NRCS related to the multi-polarization channels and evaluated along with a transect kept within the lava-affected area, is depicted in Fig. 9(d). Note that the transect has been selected to span the whole range of slopes within the lava-affected area. The co- and cross-polarized NRCS is depicted in blue and red, respectively, using continuous and dotted line for the pre- and post-event, respectively. The slope values along the transect are also annotated (see black line). The curves show that, for both the channels, the difference between pre- and post-event imagery are larger in the areas calling for lower slope. The larger slope area results in pre- and post-event NRCSs partially overlapped. This explains the odd results achieved in the high-slope area in Fig. 9(a). In scattering terms, this behavior could be explained as follows: the high-slope part is such that the lava flow does not alter in a significant way the surface scattering that dominates the surrounding environment. The low-slope area results in an accumulation zone that calls for both co- and cross-polarized backscatter larger than the pre-event case. The increasing of the cross-polarized signal is likely related to a volumetric scattering component. This makes the scattering resulting from the lava-affected area well-distinguishable from its surrounding.

To quantify the detection performance of the SP and DP features with respect to the lava footprint provided by CEMS, the following metrics are used (Corradino et al., 2019):

- accuracy (ACC) = $\sqrt{\frac{A(test \cap ref)}{A(test \cup ref)}}$
- precision (PPV) = $\sqrt{\frac{A(test \cap ref)}{A(test)}}$
- sensitivity (TPR) = $\sqrt{\frac{A(test \cap ref)}{A(ref)}}$

where A(test) and A(ref) stand for the lava flow map area obtained by the multi-polarimetric features and the reference lava flow map provided by CEMS, respectively, while A(test∩ref) and A(test∪ref), are the areas of the intersection and union between the estimated and reference lava flows, respectively. Results are listed in Table 2 and show a perfect agreement with the previous analysis. In fact, from Table 2 one can note that DP features outperform SP ones, with λ performing best.

The second test consists of the analysis of the SAR pair collected over the Nyiragongo Volcano, in the Democratic Republic of the Congo, before (13 May 2021) and after (25 May 2021) the volcanic eruption, see Table 1. An excerpt of the VV- and VH-polarized ground-projected
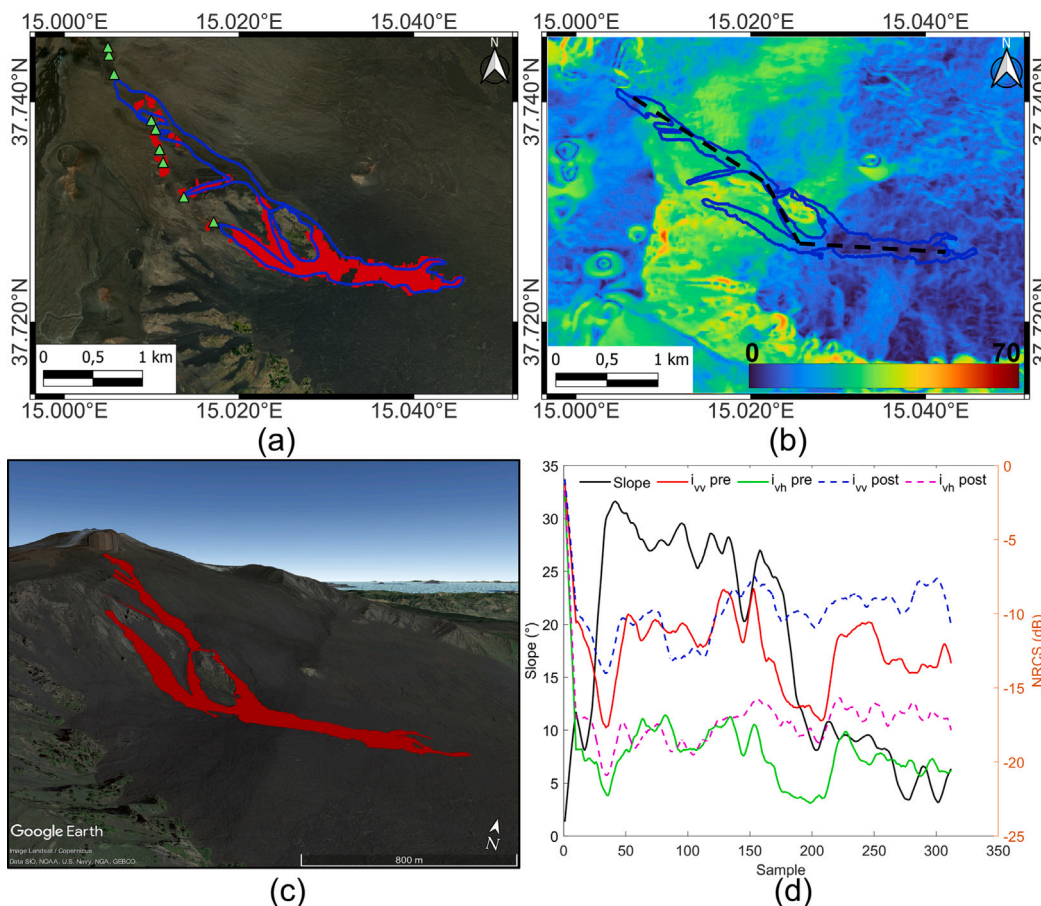
Fig. 9. Lava flow detection and slope analysis over Mount Etna: (a) The binary image is superimposed in red on the Google Earth optical image and contrasted with the Copernicus EMS lava flow footprint (shown in blue). The green triangles stand for volcanic vents; (b) Slopes evaluated using the 30 m SRTM DEM; (c) Google Earth© three-dimensional reconstruction of Mount Etna; (d) pre- (continuous line) and post-event (dotted line) co- (blue) and cross-polarized (red) NRCS evaluated along with a transect kept within the EMS footprint. The transect are annotated using the black line. (For interpretation of the references to color in this figure legend, the reader is referred to the web version of this article.)

Table 2
ACC, PPV and TPR quantitative metrics evaluated over the Etna case study.

Feature	ACC	PPV	TPR
λ	0.65	0.77	0.78
λ_1	0.54	0.77	0.60
λ_2	0.48	0.83	0.51
$R_{i_{VV}}$	0.41	0.84	0.42
$R_{i_{VH}}$	0.26	0.8	0.27
$R_{i_{VVVH}}$	0.34	0.86	0.35

NRCS image is shown in Fig. 3, where the area affected by the lava flow is enclosed in the red EMS footprint in both the pre- and post-event imagery. Again, the visual inspection of the pre- and post-event imagery does not allow a straightforward identification of the lava flow. By jointly using the images of Figs. 1 and 3 one can note differences in the backscattered signal associated with the volcanic eruption. Those differences are remarkable in the cross-polarized channel (second row) that calls for a reduced backscatter over the lava. It is hard to see differences in the co-polarized imagery (first row). This behavior makes this showcase very different from the previous one and the difference is mainly due to the fact that here the lava flow is in a vegetated area. The reduction of the cross-polarized backscatter resulting from the lava-affected area is linked to the burning of the vegetation. The latter, typically, calls for a large cross-polarized backscatter that, therefore, is strongly reduced by the burning event related to the lava.

The DP metrics λ_1, λ_2 and λ are shown in Fig. 10(a), (b) and (c), respectively, where the area affected by the changes is visible in the red

EMS footprint. The visual inspection confirms the key role played by the cross-polarized channel to distinguish the lava from the vegetated background (see the λ_2 image depicted in the panel (b)). The lava flow can be hardly observed in the λ_1 image that mostly accounts for the co-polarized backscattering. It is also worth noting that the lava-affected area appears darker than the background. This indicates that the mechanisms that rules the detection of the lava flow with respect to its surrounding is here based on the reduction of the volumetric backscattering resulting from the vegetated area. This behavior is also visible in the SP imagery that refer to the metrics $R_{i_{vv}}$, $R_{i_{vh}}$, and $R_{i_{vvvh}}$, depicted in Fig. 10(d), (e) and (f), respectively. The changes associated with the lava are mostly visible in the cross-polarized channel, while slight changes are visible in the co-polarized one and in the SPAN. The SP metric calls again for a low visual contrast between the lava and its surroundings with the exception of the $R_{i_{vh}}$ metric that provides enough separability.

By visually contrasting DP (Fig. 10(a), (b) and (c)) and SP metrics (Fig. 10(d), (e) and (f)), one can note that, even in this case, DP metrics better distinguish the lava flow with respect to the clutter than the SP ones.

To quantify the capability of multi-polarization metrics in distinguishing the lava flow from the surroundings, the TCR is used and depicted in Fig. 11(a). As suggested by Fig. 10, DP metrics do not always perform better than the SP one. The metric λ_2 and λ perform best; while $R_{i_{vh}}$ performs better than λ_1 and sightly worse than λ. The metric λ_2 guarantees a separability about 2 dB larger than SP metrics and, therefore, even in this scenario DP information results
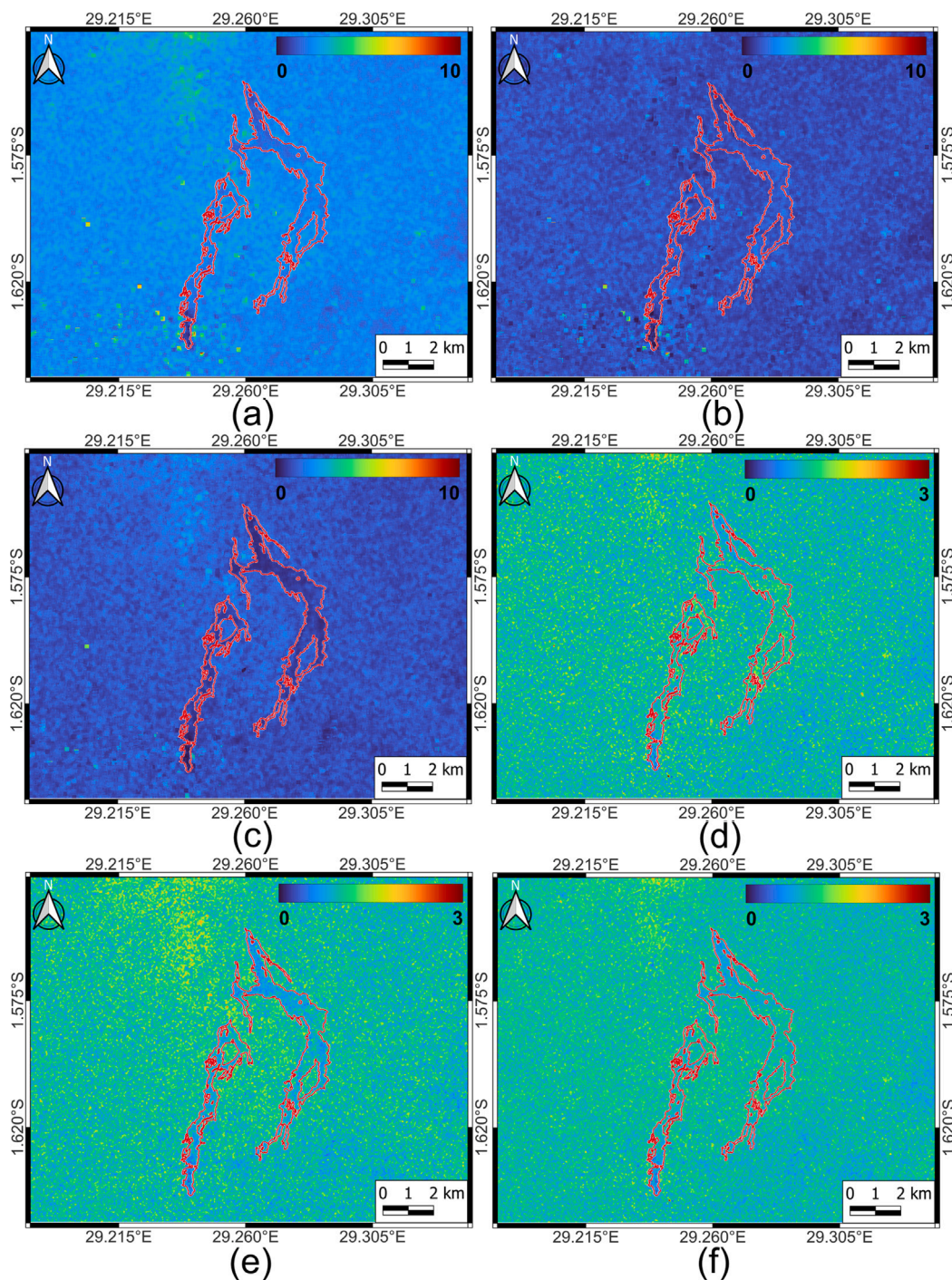
Fig. 10. False color change detection map that refers to an excerpt of the SAR acquisitions over the Mount Nyiragongo: (a) λ; (b) λ_1; (c) λ_2; (d) $R_{I_{VV}}$; (e) $R_{I_{VH}}$; and (f) $R_{I_{VVVH}}$. The lava flow area is enclosed in the red EMS footprint. (For interpretation of the references to color in this figure legend, the reader is referred to the web version of this article.)

in an advantage with respect to SP measurements. The separability between the lava and its surroundings is discussed statistically for all the metrics using the Wasserstein distance in Fig. 11b which shows that λ_2 and λ result in a similar separation with λ_2 confirming its best performance. Therefore, the CFAR is applied to λ_2, whit th evaluated using a P_{fa} equal to 10^{-5}. Artefacts and holes are removed also in this test case by applying a morphological filter. The binary image output is superimposed in red on the optical image and shown in Fig. 12(a) where, once again, a good spatial agreement with the reference lava flow depicted in black can be observed. The lava flow is well-detected almost everywhere showing that the detector performance improves with respect to the previous case. This remarkable performance is also

due to the low slope condition that characterize the whole lava-affected area, see Fig. 12(b) where the slope extracted using the 30 m SRTM DEM is depicted. The slope in the area affected by the lava is almost always lower than 15° resulting in a limited effect on the signal in backscattering.

To contrast the detection performance of SP and DP features with respect to the lava footprint provided by CEMS, the three metrics ACC, PPV and TPR are used. Results, listed in Table 3, show that λ_2 performs best. It can be also noted that the best SP feature is the cross-polarized NRCS, in accordance with the previous analysis.
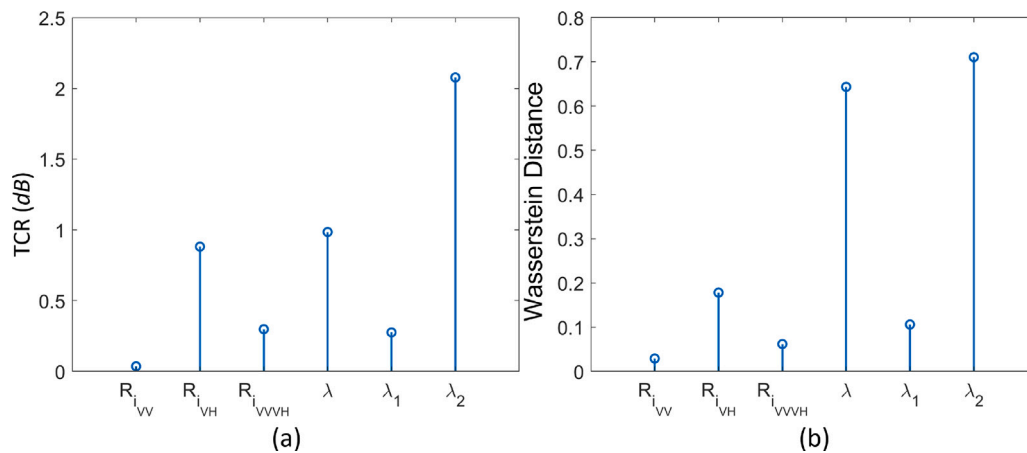
Fig. 11. TCR (a) and Wasserstein distance (b) evaluated over Mount Nyiragongo using a ROIs belonging to the lava flow and the surrounding environment.
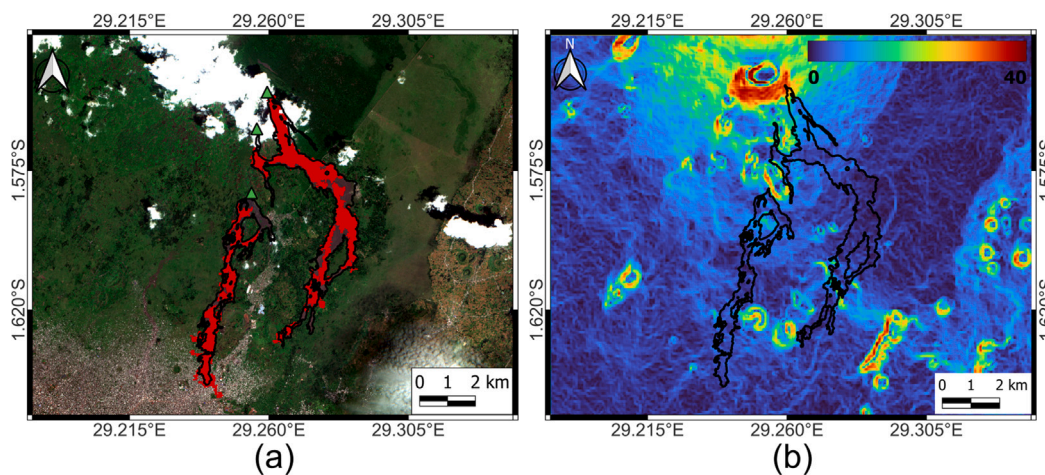

Fig. 12. Lava flow detection and slope analysis over Mount Nyiragongo: (a) The binary image is superimposed in red on the Sentinel-2 optical image and contrasted with the Copernicus EMS lava flow footprint (shown in black). The green triangles stand for volcanic vents; (b) Slopes evaluated using the 30 m SRTM DEM where positive (negative) angles stand for slopes pointing toward (away from) the SAR look direction. (For interpretation of the references to color in this figure legend, the reader is referred to the web version of this article.)

Table 3
ACC, PPV and TPR quantitative metrics evaluated over the Nyiragongo case study.

Feature	ACC	PPV	TPR
λ	0.39	0.92	0.4
λ_1	0.26	0.77	0.27
λ_2	0.75	0.9	0.8
$R_{i_{VV}}$	0.16	0.87	0.16
$R_{i_{VH}}$	0.59	0.93	0.6
$R_{i_{VVVH}}$	0.3	0.90	0.3

5. Conclusion

The role of coherent dual-polarimetric SAR measurements in observing lava flow is discussed using DP Sentinel-1 SAR imagery collected over two test cases where the lava flew over a vegetated and an unvegetated area, respectively. The dual-polarimetric analysis is carried out using a polarimetric change detector that exploits a pair of S-1 scenes collected before and after the eruption and maximizes their scattering differences using a metric based on the ratio between the pre- and post-event covariance matrices. To discuss the performance of the polarimetric change detector against external lava footprint maps, the detector output is binarized using a conventional global-threshold CFAR. In addition, the polarimetric approach is contrasted with single-polarization metrics. Experimental results show that: (a) the method

adapts in an unsupervised way to the scenario and distinguishes the lava from its surroundings; (b) the performance depends on the slope, with the best results obtained in areas characterized by low slope; (c) the scattering changes associated to the lava flow depend on the surrounding environment; (d) the DP change detector always outperforms metrics based on single-polarization channels demonstrating the superiority of polarimetric information.

From a scattering viewpoint, we also show that the discrimination of the lava against a non-vegetated background is possible because of the increased surface and volumetric scattering in the accumulation zone. In the discrimination of the lava against a vegetated background, the reduction of the volumetric scattering component resulting from the vegetation's canopy plays the dominant role.

CRediT authorship contribution statement

Emanuele Ferrentino: Conceptualization, Data curation, Formal analysis, Investigation, Methodology/Study design, Resources, Software, Supervision, Validation, Visualization, Writing – original draft, Writing – review & editing. **Christian Bignami:** Conceptualization, Funding acquisition, Investigation, Methodology/Study design, Resources, Supervision, Writing – original draft, Writing – review & editing. **Ferdinando Nunziata:** Conceptualization, Investigation, Methodology/Study design, Supervision, Writing – original draft, Writing – review & editing. **Salvatore Stramondo:**

Project administration, Supervision,Funding acquisition, Writing – original draft, Writing – review & editing. **Maurizio Migliaccio:** Project administration, Supervision, Writing – review & editing.

Declaration of competing interest

The authors declare the following financial interests/personal relationships which may be considered as potential competing interests: Emanuele Ferrentino reports was provided by National Institute of Geophysics and Volcanology.

Data availability

Data will be made available on request

References

Bignami, C., Chini, M., Amici, S., Trasatti, E., 2020. Synergic use of multi-sensor satellite data for volcanic hazards monitoring: The Fogo (Cape Verde) 2014–2015 effusive eruption. Front. Earth Sci. 8, http://dx.doi.org/10.3389/feart.2020.00022.

Bignami, C., Corradini, S., Merucci, L., de Michele, M., Raucoules, D., De Astis, G., Stramondo, S., Piedra, J., 2014. Multisensor satellite monitoring of the 2011 Puyehue-Cordon Caulle eruption. IEEE J. Sel. Top. Appl. Earth Obs. Remote Sens. 7 (7), 2786–2796. http://dx.doi.org/10.1109/JSTARS.2014.2320638.

Bignami, C., Ruch, J., Chini, M., Neri, M., Buongiorno, M.F., Hidayati, S., Sayudi, D.S., Surono, 2013. Pyroclastic density current volume estimation after the 2010 merapi volcano eruption using X-band SAR. J. Volcanol. Geotherm. Res. 261, 236–243. http://dx.doi.org/10.1016/j.jvolgeores.2013.03.023.

Bisson, M., Spinetti, C., Andronico, D., Palaseanu-Lovejoy, M., Fabrizia Buongiorno, M., Alexandrov, O., Cecere, T., 2021. Ten years of volcanic activity at Mt Etna: High-resolution mapping and accurate quantification of the morphological changes by pleiades and lidar data. Int. J. Appl. Earth Obs. Geoinf. 102, 102369. http://dx.doi.org/10.1016/j.jag.2021.102369.

Boudoire, G., Calabrese, A., Sordini, P., Habakaramo Macumu, P., Rafflin, V., Valade, S., Mweze, T., Kazadi Mwepu, J.-C., Safari Habari, F., Amani Kahamire, T., Mumbere Mutima, Y., Ngaruye, J.-C., Tuyishime, A., Tumaini Sadiki, A., Mavonga Tuluka, G., Mapendano Yalire, M., Kets, E.-D., Grassa, F., D'Alessandro, W., Caliro, S., Rufino, F., Tedesco, D., 2022. Scientific response to the 2021 eruption of nyiragongo based on the implementation of a participatory monitoring system. Sci. Rep. 12 (1), 7488. http://dx.doi.org/10.1038/s41598-022-11149-0.

Bovolo, F., Bruzzone, L., 2005. A detail-preserving scale-driven approach to change detection in multitemporal SAR images. IEEE Trans. Geosci. Remote Sens. 43 (12), 2963–2972. http://dx.doi.org/10.1109/TGRS.2005.857987.

Cannavo', F., Sciotto, M., Cannata, A., Di Grazia, G., 2019. An integrated geophysical approach to track magma intrusion: The 2018 Christmas Eve eruption at Mount Etna. Geophys. Res. Lett. 46 (14), 8009–8017. http://dx.doi.org/10.1029/2019GL083120.

CEMS, 2019. [Emsr336] etna volcano. URL: https://emergency.copernicus.eu/mapping/ems-product-component/EMSR336_01ETNAVOLCANO_01DELINEATION_MONIT01/3. Accessed=2023-08-05.

CEMS, 2021. [Emsr513] mount nyiragongo. URL: https://emergency.copernicus.eu/mapping/ems-product-component/EMSR513_AOI01_GRA_MONIT02_r1_RTP01/3. Accessed=2023-08-05.

Corradino, C., Bilotta, G., Cappello, A., Fortuna, L., Del Negro, C., 2021. Combining radar and optical satellite imagery with machine learning to map lava flows at mount etna and fogo island. Energies 14 (1), http://dx.doi.org/10.3390/en14010197.

Corradino, C., Ganci, G., Cappello, A., Bilotta, G., Hérault, A., Del Negro, C., 2019. Mapping recent lava flows at mount etna using multispectral sentinel-2 images and machine learning techniques. Remote Sens. 11 (16), http://dx.doi.org/10.3390/rs11161916, URL: https://www.mdpi.com/2072-4292/11/16/1916.

Dietterich, H.R., Poland, M.P., Schmidt, D.A., Cashman, K.V., Sherrod, D.R., Espinosa, A.T., 2012. Tracking lava flow emplacement on the east rift zone of kīlauea, hawai'i, with synthetic aperture radar coherence. Geochem. Geophys. Geosyst. 13 (5), http://dx.doi.org/10.1029/2011GC004016.

Dualeh, E.W., Ebmeier, S.K., Wright, T.J., Albino, F., Naismith, A., Biggs, J., Ordoñez, P.A., Boogher, R.M., Roca, A., 2021. Analyzing explosive volcanic deposits from satellite-based radar backscatter, Volcán de Fuego, 2018. J. Geophys. Res.: Solid Earth 126 (9), http://dx.doi.org/10.1029/2021JB022250.

Ferrentino, E., Marino, A., Nunziata, F., Migliaccio, M., 2019a. A dual–polarimetric approach to earthquake damage assessment. Int. J. Remote Sens. 40 (1), 197–217. http://dx.doi.org/10.1080/01431161.2018.1511935.

Ferrentino, E., Nunziata, F., Bignami, C., Graziani, L., Maramai, A., Migliaccio, M., 2021. Multi-polarization C-band SAR imagery to quantify damage levels due to the central Italy earthquake. Int. J. Remote Sens. 42 (15), 5969–5984. http://dx.doi.org/10.1080/01431161.2021.1933247.

Ferrentino, E., Nunziata, F., Bignami, C., Graziani, L., Maramai, A., Migliaccio, M., Stramondo, S., 2022. On the combination of dual-polarization sentinel-1 ascending/descending orbiting passes to estimate damage due to the 2016 central Italy earthquake. IEEE J. Sel. Top. Appl. Earth Obs. Remote Sens. 15, 9509–9518. http://dx.doi.org/10.1109/JSTARS.2022.3217889.

Ferrentino, E., Nunziata, F., Marino, A., Migliaccio, M., Li, X., 2019b. Detection of wind turbines in intertidal areas using SAR polarimetry. IEEE Geosci. Remote Sens. Lett. 16 (10), 1516–1520. http://dx.doi.org/10.1109/LGRS.2019.2905714.

Lee, J.-Y., Jung, S.-W., Hong, S.-H., 2023. Mapping lava flow from the Kilauea eruption of 2018 in the east rift zone using space-based synthetic aperture radar. GISci. Remote Sens. 60 (1), 2176275. http://dx.doi.org/10.1080/15481603.2023.2176275.

Marino, A., Nannini, M., 2022. Signal models for changes in polarimetric SAR data. IEEE Trans. Geosci. Remote Sens. 60, 1–18. http://dx.doi.org/10.1109/TGRS.2021.3113182.

Migliaccio, M., Nunziata, F., 2014. On the exploitation of polarimetric SAR data to map damping properties of the deepwater horizon oil spill. Int. J. Remote Sens. 35 (10), 3499–3519. http://dx.doi.org/10.1080/01431161.2014.905730.

Migliaccio, M., Nunziata, F., Marino, A., Brekke, C., Skrunes, S., 2021. Ocean applications. In: Hajnsek, I., Desnos, Y.-L. (Eds.), Polarimetric Synthetic Aperture Radar: Principles and Application. Springer International Publishing, Cham, pp. 255–277. http://dx.doi.org/10.1007/978-3-030-56504-6_6.

Migliaccio, M., Nunziata, F., Montuori, A., Brown, C., 2011. Marine added-value products using RADARSAT-2 fine quad-polarization. Can. J. Remote Sens. 37 (5), 443–451. http://dx.doi.org/10.5589/m11-054.

Muhammad, A., Buono, A., Nunziata, F., Ferrentino, E., Velotto, D., Migliaccio, M., 2022. On the effects of the incidence angle on the L-band multi-polarisation scattering of a small ship. Remote Sens. 14 (22), http://dx.doi.org/10.3390/rs14225813.

Nunziata, F., de Macedo, C.R., Buono, A., Velotto, D., Migliaccio, M., 2019. On the analysis of a time series of X–band TerraSAR–X SAR imagery over oil seepages. Int. J. Remote Sens. 40 (9), 3623–3646. http://dx.doi.org/10.1080/01431161.2018.1547933.

Palamà, R., Monserrat, O., Crippa, B., Crosetto, M., Bru, G., Ezquerro, P., Bejar-Pizarro, M., 2023. Radargrammetry DEM generation using high-resolution SAR imagery over la palma during the 2021 cumbre vieja volcanic eruption. IEEE Geosci. Remote Sens. Lett. 20, 1–5. http://dx.doi.org/10.1109/LGRS.2023.3238182.

Plank, S., Shevchenko, A.V., d'Angelo, P., Gstaiger, V., González, P.J., Cesca, S., Martinis, S., Walter, T.R., 2023. Combining thermal, tri-stereo optical and bi-static InSAR satellite imagery for lava volume estimates: the 2021 Cumbre Vieja eruption, La Palma. Sci. Rep. 13 (1), 2057. http://dx.doi.org/10.1038/s41598-023-29061-6.

Poland, M.P., 2022. Synthetic aperture radar volcanic flow maps (SAR VFMs): a simple method for rapid identification and mapping of volcanic mass flows. Bull. Volcanol. 84 (3), 32. http://dx.doi.org/10.1007/s00445-022-01539-7.

Polcari, M., Ferrentino, E., Bignami, C., Borgstrom, S., Nappi, R., Siniscalchi, V., 2023. SAR data for detecting landslide phenomena: The november 26, 2022 landslide of the Ischia island (southern Italy). IEEE J. Sel. Top. Appl. Earth Obs. Remote Sens. 16, 5686–5694. http://dx.doi.org/10.1109/JSTARS.2023.3286993.

Rogic, N., Charbonnier, S.J., Garin, F., Dayhoff, II, G.W., Gagliano, E., Rodgers, M., Connor, C.B., Varma, S., Shean, D., 2023. Characterizing and mapping volcanic flow deposits on mount st. Helens via dual-band SAR imagery. Remote Sens. 15 (11), http://dx.doi.org/10.3390/rs15112791.

Solikhin, A., Pinel, V., Vandemeulebrouck, J., Thouret, J.-C., Hendrasto, M., 2015. Mapping the 2010 merapi pyroclastic deposits using dual-polarization synthetic aperture radar (SAR) data. Remote Sens. Environ. 158, 180–192. http://dx.doi.org/10.1016/j.rse.2014.11.002.

Vallender, S.S., 1974. Calculation of the Wasserstein distance between probability distributions on the line. Theory Probab. Appl. 18 (4), 784–786. http://dx.doi.org/10.1137/1118101.

Weissel, J.K., Czuchlewski, K.R., Kim, Y., 2004. Synthetic aperture radar (SAR)-based mapping of volcanic flows: Manam island, Papua New Guinea. Nat. Hazards Earth Syst. Sci. 4 (2), 339–346. http://dx.doi.org/10.5194/nhess-4-339-2004.

Zebker, H.A., Rosen, P., Hensley, S., Mouginis-Mark, P.J., 1996. Analysis of active lava flows on Kilauea volcano, Hawaii, using SIR-C radar correlation measurements. Geology 24 (6), 495–498. http://dx.doi.org/10.1130/0091-7613(1996)024<0495:AOALFO>2.3.CO;2.